Journal of Materials Chemistry A

Accepted Manuscript

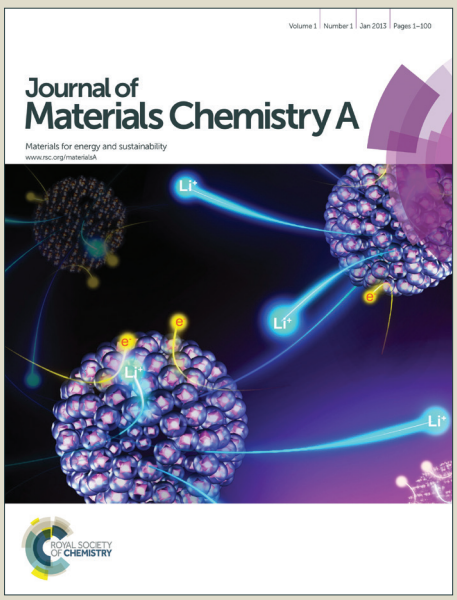

ROYAL SOCIETY OF CHEMISTRY

www.rsc.org/materialsA

Journal of Materials Chemistry A RSCPublishing

ARTICLE

Efficient Titanium Nitride/Titanium Oxide Composite Photoanodes for Dye-Sensitized Solar Cells and Water Splitting

Cite this: DOI: 10.1039/x0xx00000x

Received 00th January 2014,
Accepted 00th January 2014

DOI: 10.1039/x0xx00000x

www.rsc.org/

Chun–Ting Li,[a] Sie–Rong Li,[b] Ling–Yu Chang,[c] Chuan–Pei Lee,[a] Pei–Yu Chen,[a] Shih–Sheng Sun,[b,*] Jiang–Jen Lin,[c,*] R. Vittal,[a] and Kuo–Chuan Ho[a,c,*]

Efficient titanium nitride/titanium oxide (TiN/TiO_2) composite photoanodes were proposed for the use not only in dye-sensitized solar cells (DSSCs) but also in water splitting. When the TiN precursor films were sintered at 500 °C for 0.5 to 4 h, they were partially converted to TiO_2 crystalline containing both rutile and anatase phases. For the DSSCs, higher TiN content in the photoanodes possesses more negative flat-band potential and higher conductivity but lower surface area for the dye adsorption; therefore the increase in V_{OC} and *FF* but the decrease in J_{SC} value were observed, respectively. The best DSSC with TiN/TiO_2 composite photoanode annealed for 1 h exhibited a power conversion efficiency of 7.27%, while the cell without TiN, *i.e.*, the cell with a standard P25 photoanode, showed an efficiency of 7.02%. For the water splitting, higher TiN content in the photoanodes would better triggering the H_2O electrolysis, but the less photo-induced current response at UV light illumination. Considering the water splitting performance measured at AM 1.5G, the TiN/TiO_2 composite photoanode annealed for 1 h showed the best photo-induced current density (J_{pho}) of 0.12 mA cm^{-2}, as compared with that of the standard P25 film. With the TiN/TiO_2 composite photoanode annealed for 1 h, both DSSCs and water splitting electrochemical devices achieved their best performance independently.

Introduction

Titanium nitride (TiN) is an important functional material and has several attractive properties; for instant, it exhibits high hardness, excellent thermal and electrical conductivity, good chemical stability and biocompatibility, good corrosion resistance, and high absorption in the visible light range[1-4]. Titanium nitride-based thin films have been proposed for many applications, including nitrite detection[5], pollution degradation[6, 7], heterojuntion photovoltaics[8], resonators[9-11], biosensors[12-14], DNA sequencing electrodes[15], fuel cells[16-19], water splitting[20-23], supercapacitors[24-26], superconductors[27-29], lithium batteries[30-32], field effect transistors[33], and dye-sensitized solar cells.[6, 34-42]

Nowadays, the severe energy shortage points out the urgency for developing the sustainable and clean energy resources. Among various kinds of clean energy, solar energy is considered as promising renewable power supplement without limitation since it can be converted into electrical, chemical or thermal energy. In this regard, dye–sensitized solar cells (DSSCs) are the solar-to-electrical conversion devices and have been attracting great attention in recent years. They have been extensively investigated since 1991[43], owing to their outstanding advantages, *e.g.,* low-cost production possibility, good compatibility to environment, and high conversion efficiency. A DSSC usually consists of three key parts: a dye-adsorbed TiO_2 film as the photoanode, an electrolyte with the redox couple of iodide/triiodide (I^-/I_3^-), and a platinum-coated counter electrode (Pt-CE). Among these, the TiO_2 plays a very important role in providing large surface area for the dye adsorption and in transferring the electrons to the outer circuit. Therefore, crystallinity, conductivity, and porosity of the TiO_2 film can affect the performance of the DSSC. The inherent conductivity of a TiO_2 film is very low, and results in poor electron transport through the film to the fluorine-doped tin oxide (FTO) conducting substrate. The cell efficiency is therefore limited by overwhelming interfacial recombination reactions between the excited electrons and I_3^- ions. Many researchers introduced a number of additives with high conductivity, including gold nanoparticles,[44, 45] silver nanoparticles,[46] carbon-based materials,[47-49] transition-metal-based materials,[50, 51] into the TiO_2 films to enhance their electrical conductivity and retard the charge recombination

reactions. Yoo *et al.* introduced TiN as a charge collector to cover onto the TiO_2 layer in a transparent conducting oxide (TCO)-less photoanode (a special design);[52] the TiN has successfully retarded the recombination between the injected electrons and I_3^- ions. Lee *et al.* incorporated pristine TiN and thermally-treated TiN (tt-TiN) nanoparticles into binder-free TiO_2 films to enhance physical-necking between the TiO_2 particles.[34] Sun *et al.* applied nitrogen doped titanium dioxide (N-TiO_2) and nitrogen-carbon co-doped titanium dioxide (CN-TiO_2) photoanodes for DSSCs;[6] the DSSCs with N-TiO_2 and CN-TiO_2 photoanodes exhibited power conversion efficiencies (η) of 2.44% and 3.31%, respectively, which are higher than that of the DSSC with standard P25 photoanode (1.61%).

On the other hand, solar-to-chemical conversion is usually accomplished in terms of hydrogen production via water splitting through a photoelectrochemical reaction. The electrochemical cell for water splitting is similar to a DSSC; it also contains three important parts: a photocatalytic semiconductor film as the photoanode, an electrolyte, and a counter electrode (CE)[53]. Instead of using the dye in a DSSC, the semiconductor film generates photoelectrons and holes in an electrochemical cell for water splitting. The photoelectrons then trigger the production of H_2 (water reduction) at the CE/electrolyte interface; simultaneously the holes trigger water oxidation to produce O_2 at the photoanode's surface. Generally, the performance of a photocatalyst (semiconductor film) could be limited by its energy band gap, crystallinity, conductivity, porosity, and stability. Numerous investigations have been made to develop efficient photocatalysts with low energy band gap, high conductivity, and large porosity, intending to retard photoelectron–hole recombination[54-57]. Maeda *et al.* applied titanium fluorooxynitride ($TiN_xO_yF_z$) powder as the photocatalyst for water oxidation in the presence of silver nitrate as the sacrificial electron acceptor;[23] the nitrogen content in $TiN_xO_yF_z$ was reported to be responsible for a broad photocatalytic activity in the visible light region. Chen *et al.* used F-TiO_2 and TiN/F-TiO_2 nanoparticles as the consuming photocatalysts for water-photooxidation[21]. The photocatalytic activity of TiN/F-TiO_2 was found to be higher than those of TiO_2 and F-TiO_2, due to two reasons: (1) the red shift in the absorption spectra introduced by the additional TiN nanoparticles; (2) the more efficient separation between the photo-induced electrons and holes provided by the additional Ti^{3+} reactive center on the TiN surface. Li *et al.* synthesized the solid, yolk–shell, and hollow TiN microspheres separately, and applied them as visible light-induced photocatalysts for water splitting[20]. They achieved good photo-induced current densities of 0.020, 0.035, and 0.030 mA cm^{-2} for the solid, yolk–shell, and hollow TiN photocatalysts, respectively. TiN microspheres provide narrow energy band gap for visible light absorption, high surface area, good stability, and excellent electrical conductivity, which facilitated light harvesting and thereby enhanced photo-induced current density by suppressing photoelectron–hole recombination.

According to the literatures mentioned above, we aim in this study to prepare the effective TiN-based thin films as the photoanode for two kinds of clean energy applications, namely the DSSCs and water splitting separately. A simple doctor blade procedure followed by a post-annealing treatment is successfully introduced. By applying thermal treatment at 500 ^oC for different periods, TiN films could be partially converted to TiO_2 crystalline, and the composite films containing both TiN and TiO_2 crystallines are applied as the photoanodes for the DSSCs or for water splitting separately. We explore several key parameters, including the conductivity and the flat-band potential of the films, to determine the best performance for both applications.

Experimental

Materials

Titanium (IV) tetraisoproproxide (TTIP, > 98%), ethanol (EtOH, 99.5%), isopropyl alcohol (IPA, 99.5%), and 2–methoxyethanol (≥ 99.5%) were obtained from Sigma Aldrich. Lithium iodide (LiI, synthetic grade) and iodine (I_2, synthetic grade) were purchased from Merck. Acetone (99+%), 4–tert–butylpyridine (tBP, 96%), and tert–butyl alcohol (tBA, 96%) were supplied by Acros. 3–methoxypropionitrile (MPN, 99%) was received from Fluka. 1,2–dimethyl–3–propylimidazolium iodide (DMPII) and 25 μm–thick Surlyn® (SX1170–25) were bought from Solaronix (S.A., Aubonne, Switzerland). Potassium sulfate (K_2SO_4, 99.99%), acetonitrile (ACN, 99.99%), nitric acid (HNO_3, *ca.* 65% solution in water), and dichloromethane (DCM, 99.99%) were procured from J. T. Baker. Titanium nitride nanoparticles (TiN, 99.9%, 50 nm) were acquired from Wako. Commercial titanium dioxide nanoparticles (P25, 99.9%, 20 nm, UR-ITIT001) were obtained from UniRegion Bio-Tech. Indium-doped tin oxide (ITO, 10 Ω $sq.^{-1}$, UR-ITO007-0.7 mm) conducting glasses were provided by Uni-onward Corp., Taiwan. Fluorine–doped SnO_2 (FTO, TEC-7, 7 Ω $sq.^{-1}$) conducting glasses were delivered by NSG America, Inc., New Jersey, USA.

Fabrication and characterization of TiN films

ITO and FTO conducting glasses were first cleaned with a neutral cleaner and then washed with deionized water (DIW), acetone, and isopropanol sequentially. A standard TiO_2 paste was prepared by adding 15 wt% of commercial P25 nanoparticles and 15 wt% of home-made polymeric dispersant, poly(oxyethylene)-segmented imide (POEM), into DIW/EtOH (at the volume ratio of 7/3). The TiN paste contained 15 wt% of TiN nanoparticles and 15 wt% of POEM in DIW/EtOH (volume ratio = 7/3). The dispersant, POEM, was prepared according to our previous report[58, 59] by the procedure shown in **Scheme S1**, and was used to control the pore diameters in the films and to prevent the films from being cracked during drying. Then, the TiO_2 film and TiN-based film were prepared by using the P25 paste and TiN paste, respectively. First of all, the FTO conducting surface was spin-coated a 100 nm-compact

layer by using a mixture solution of TTIP/2–methoxyethanol (at the weight ratio of 1/3). The porous TiO_2 (P25) film and TiN-based films were coated on the treated FTO glasses, each for a thickness of 12 μm, by using a doctor blade technique. The P25 films were sintered at 500 ^oC for 30 min in air, and the TiN-based films were sintered at 500 ^oC for 0.5 to 4 h in air. The photoanodes are designated as P25, TiN/TiO_2-0.5h, TiN/TiO_2-1h, TiN/TiO_2-2h, TiN/TiO_2-4h separately.

The surface areas of P25 and TiN nanoparticles were quantified by Brunauer–Emmett–Teller (BET, ASAP2010, Micromeritics, USA) measurements. Dispersion of the TiN nanparticles in POEM aqueous solution was examined by using an UV-vis-NIR spectrophotometer (JASCO V-670, USA). To find out the crystalline phases of the P25 and all TiN/TiO_2 composite films, an X-ray diffraction (XRD, Rigaku, Tokyo, Japan) technique was used. A field–emission scanning electron microscope (FE–SEM, Nova NanoSEM 230, FEI, Oregon, USA), coupled with an energy dispersive X-ray spectroscope (EDX, Oxford INCA x-act), was applied for observing the surface morphology of the films. A four-point probe technique was employed to obtain the conductivities of the films; the conductivities were recorded by a Keithley's instrument (Keithley 2400, Keithley Instruments Inc., USA).

Fabrication of DSSCs

After the sintering process, the P25 and all TiN/TiO_2 composite films were patterned for an area of 0.16 cm^2 and were immersed in a DCM-based 5×10^{-4} M CR147 dye solution, at room temperature for 24 h, to obtain P25 and TiN/TiO_2 composites photoanodes. The new non-commercial CR147 dye, represented in **Scheme S2**, is a very efficient organic dye[60, 61]. A standard platinum (Pt) CE was prepared by direct current sputtering a Pt thin film on an ITO substrate for a thickness of 50 nm. Then the photoanode was coupled with the platinum counter electrode (Pt-CE), keeping a fixed gap of 25 μm between the two electrodes, by using a heated 25 μm–thick Surlyn® film. The electrolyte, containing 0.7 M DMPII, 0.038 M I_2, and 0.5 M TBP in MPN/ACN with a volume ratio of 1/1, was injected into the gap between the electrodes by capillarity.

Evaluation of DSSCs performance

The performances of the DSSCs with different photoanodes were evaluated by a potentiostat/galvanostat (PGSTAT 30, Autolab, Eco-Chemie, the Netherlands), under 100 mW cm^{-2} light illumination, by using a class A quality solar simulator (XES–301S, AM1.5G, San–Ei Electric Co., Ltd., Osaka, Japan). The incident light intensity was calibrated with a standard Si cell (PECSI01, Peccell Technologies, Inc., Kanagawa, Japan). The incident photon–to–current conversion efficiencies (IPCE) of the DSSCs with various photoanodes were obtained by the potentiostat/galvanostat and another class A quality solar simulator (PEC–L11, AM1.5G, Peccell Technologies, Inc., Kanagawa, Japan), equipped with a monochromator (model 74100, Oriel Instrument, California, USA). The incident radiation flux (φ) was obtained by using an optical detector (model 71580, Oriel Instrument, California, USA) and a power meter (model 70310, Oriel Instrument, California, USA). Electrochemical properties of the DSSCs were measured by electrochemical impedance spectroscopy (EIS). EIS spectra were obtained by the above-mentioned potentiostat/galvanostat, equipped with an FRA2 module; the explored frequency range was from 10 mHz to 65 kHz, and the corresponding ac amplitude was 10 mV. Under 100 mW cm^{-2} light illumination, the applied bias for a DSSC was set at its open-circuit voltage. Under dark condition, the applied bias for all DSSCs was set at –0.80 V. The impedance spectra were analysed by using an equivalent circuit model.[62] Moreover, the dye loading amounts on the films were measured following several steps as follows: (1) five bottles of CR147 dye solutions with the same dye concentration (5×10^{-4} M) were prepared; (2) the P25 TiO_2 film and four different TiN/TiO_2 composite films (1 cm^2, with a thickness of 12 μm) were immersed in the dye-solutions; (3) the dye-adsorbed films were removed after 24 h; (4) the absorption spectra of the residual dye solutions were measured by using an UV-vis-NIR spectrophotometer (**Fig. S1a**); (5) pertinent absorption intensities were obtained at 483 nm (the λ_{max} of CR147); (6) the concentrations of the dyes were determined by using the calibration curve of standard CR147 solution (**Fig. S1b**); the difference between the concentrations of the dyes in the original solution (5×10^{-4} M) and residual solution gives the dye loading amount on a film.

Evaluation of water splitting performance

The performance of the photoanodes for water splitting could be estimated by measuring the photo-induced current densities of their electrochemical cells. The photo-induced current densities were measured by the potentiostat/galvanostat (PGSTAT 30, Autolab, Eco-Chemie, the Netherlands) in a three-electrode electrochemical system. The P25 and TiN/TiO_2 composite films (1 cm^2) were used as the working electrodes; a Pt foil and a Ag/AgCl electrode were used as the counter and reference electrodes, respectively. The electrolyte was an aqueous solution (pH=7) containing 0.5 M K_2SO_4 as the supporting electrolyte. The measurements were carried out under the following conditions: (1) a 35 mW cm^{-2} ultraviolet light (UV) illumination by an UV light generator (filter: 320~500 nm, OmniCure Series 1000, EXFO Photonic Solutions Inc., Canada), and (2) a 100 mW cm^{-2} sun light illumination by a class A quality solar simulator (PEC–L11, AM1.5G, Peccell Technologies, Inc., Kanagawa, Japan). The incident light intensity was calibrated with the same standard Si cell mentioned above. Energy band gaps of the TiO_2 and TiN/TiO_2 composite films were determined by using their absorption and transmittance spectra, which were obtained by the UV-vis-NIR spectrophotometer, equipped with an integrating sphere. Flat band potentials of the films were estimated from their Mott–Schottky plots, obtained by using the same three-electrode electrochemical system mentioned above. The potentiostat/galvanostat (PGSTAT 900B, Autolab, Eco-

Chemie, the Netherlands), equipped with a frequency response analyser, was used to obtain the Mott–Schottky plots.

Results and Discussion

Surface area and dispersibility of TiN and P25 nanoparticles

A specific surface area analyser was used to obtain Brunauer–Emmett–Teller (BET) adsorption/desorption curves of TiN and P25 by nitrogen gas adsorption. In **Fig. S2**, it can be clearly seen that the TiN nanoparticles (TiN-NPs, 50 nm) adsorb lower amount of nitrogen than that of P25 nanoparticles (P25-NPs, 20 nm). The BET surface area was calculated to be 25.66 m^2 g^{-1} for TiN-NPs and 44.74 m^2 g^{-1} for P25-NPs, *i.e.*, the surface area of TiN-NPs is only 0.57 times that of P25-NPs. On the other hand, the dispersibility of pristine TiN-NPs could be tested by using UV-vis-NIR spectra of two aqueous solutions containing TiN or TiN/POEM separately. **Fig. S3** shows the plots of normalized absorption at 730 nm versus time for both solutions. It can be seen that the aqueous solution containing only TiN-NPs shows an absorption decrease of 38% after 6 h, whereas the aqueous solution containing TiN/POEM does not show any absorption decrease after the same period. In the case of TiN/POEM, the absorption remained roughly constant because the TiN-NPs kept well distributed and intact in it. Without the present of POEM, TiN-NPs settled down after 6 h, and the absorption decreased owing to the absence of most of TiN-NPs in the path of UV-vis light. It is thus clear that the home-made POEM polymer is an effective dispersant for TiN-NPs.

Morphology

Fig. 1 shows plane view FE-SEM images of the films of pre-annealed TiN, TiN/TiO_2-0.5h, TiN/TiO_2-1h, TiN/TiO_2-2h, TiN/TiO_2-4h, and P25. In **Fig. 1a**, the pre-annealed TiN film shows a porous structure but rather loose connection among the TiN-NPs. The necking of particles in other films appears to be slightly better than that in the pristine TiN film; it is well known that annealing of a TiO_2 film below 500 ^oC improves the necking among the particles of the film. From **Fig. 1b** to **1e**, all the annealed TiN/TiO_2 composite films maintain a three dimensional porous structure without any aggregation and combination of TiN/TiO_2-NPs, which perfectly fit in the demands of the photoanodes for DSSCs or for water splitting. Therefore, it can be verified that the home-made POEM polymer dispersant not only can provide great dispersion ability to TiN-NPs, but also prevent its aggregation and combination during the post-thermal process. A similar porous structure for the standard P25 film was also observed as seen in **Fig. 1f**. Note that the TiN/TiO_2 composite films and P25 film all exhibit a thickness of 12 μm. **Fig. S4a** and **S4b** show cross-sectional FE-SEM images of a TiN/TiO_2 composite film and of the P25 film, respectively. Moreover, the coverage of TiO_2 component on the surface of the TiN/TiO_2 composite film was investigated by an elemental mapping technique, using an EDX spectroscope. As shown in **Fig. S5**, the red dots represent the signals of oxygen, which refer to the formation of TiO_2, while the green dots represent the signals of nitrogen, which refer to the residual TiN. Here, each element is detected at its K atomic orbital. On all TiN/TiO_2 composite films, both oxygen and nitrogen are distributed uniformly. Increase of annealing period of a composite film increases its content of oxygen and decreases its content of nitrogen.

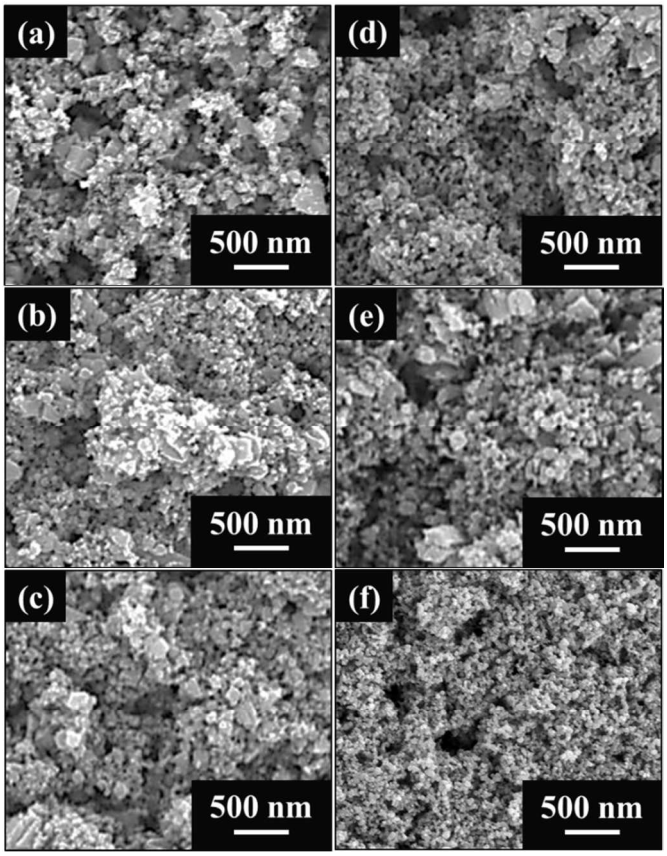

Fig. 1 Plane view FE-SEM images of films of (a) pre-anneal TiN, (b) TiN/TiO_2-0.5h, (c) TiN/TiO_2-1h, (d) TiN/TiO_2-2h, (e) TiN/TiO_2-4h, and (f) P25.

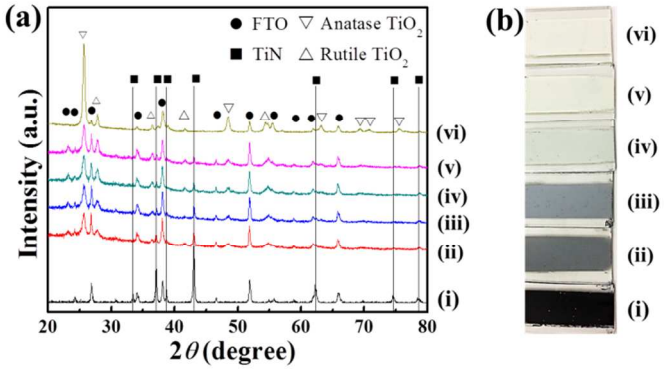

Fig. 2 (a) XRD patterns and (b) photographs of the films of (i) pre-anneal TiN, (ii) TiN/TiO_2-0.5h, (iii) TiN/TiO_2-1h, (iv) TiN/TiO_2-2h, (v) TiN/TiO_2-4h, and (vi) P25.

X-ray diffraction patterns

In **Fig. 2**, the pre-annealed TiN film shows strong peaks at the 2θ values of 33.43°, 37.18°, 38.65°, 43.03°, 62.21°, 74.41°, and 78.44°, which correspond to a pure TiN cubic crystalline according to JCPDS card No. 02-1221. With increasing the annealing period, all the annealed TiN/TiO_2 composite films show an obvious deceasing in the peaks of TiN crystalline and the increasing in the peaks referring to the TiO_2 crystalline, containing both anatase and rutile crystal phases simultaneously. It is clear that the TiN crystalline transform into TiO_2 crystalline in all the annealed TiN/TiO_2 composite films. The TiN-transformed anatase TiO_2 can be confirmed by the peaks at the 2θ values of 25.67° and 48.79°, which correspond to the tetragonal crystal planes of (101) and (200), respectively (JCPDS card No. 75-1537). The TiN-transformed rutile TiO_2 can be confirmed by the peaks at the 2θ values of 27.87°, 36.43°, 41.72°, and 54.98°, which correspond to the tetragonal crystal planes of (110), (101), (111), and (211), respectively (JCPDS card No. 88-1175). The standard P25 film also exhibits TiO_2 crystalline with both anatase and rutile crystal phases. Furthermore, the conversion degree of an annealed TiN/TiO_2 composite film could be estimated by comparing the peak intensity of the TiN primary (200) crystal plane with that of the pre-annealed film. The conversion degrees were found to be 57.10%, 71.18%, 84.57%, and 86.77% at the annealing periods of 0.5, 1, 2, and 4 h, respectively. At the annealing period of 4 h, the crystal phase of TiN/TiO_2-4h film is nearly the same as that of P25 film. On the other hand, an interesting color change of the TiN/TiO_2 composite films with different annealing periods are observed and shown correspondingly in the photographs nearby the XRD patterns in **Fig. 2**. The pre-annealed TiN film (annealed for 0 h) shows a uniform dark blue surface without any cracks. With increasing annealing time, the film color changes from dark blue to white; this change is in consistency with the crystalline phase transformation of all TiN/TiO_2 composite films. The standard P25 film shows a uniform white surface without any cracks.

Optical spectra

The absorption and transmittance spectra of the films of TiN/TiO_2-0.5h, TiN/TiO_2-1h, TiN/TiO_2-2h, TiN/TiO_2-4h, and P25, were measured in the wavelength range of 300–800 nm and shown in **Fig. 3**. In **Fig. 3a**, all TiN/TiO_2 composite films and the P25 film show one set of absorption peaks in a wavelength range from 300 to 400 nm, which corresponds to the TiO_2 contents (prefer UV absorption) of the films. Another set of absorption waves from 400 to 800 nm and corresponds to the TiN contents (prefer visible absorption) in the films. In brief, the higher TiN contents in the films cause higher visible light absorption; this phenomenon may be attributed to the narrower energy band gap[20] and the plasmonic effect provided by TiN[63-65]. In **Fig. 3b**, the transmittance of a TiN/TiO_2 composite film decreases with increasing content of the TiN, which agrees well with the absorption behavior of the film.

DSSCs performance

Photocurrent density–voltage characteristics of the DSSCs with various photoanodes are shown in **Fig. 4a**. At 100 mW cm^{-2} (AM 1.5G) illumination, the P25 photoanode adsorbed with CR147 rendered its DSSC a conversion efficiency of 7.02%. As summarized in **Table 1**, all the DSSCs with TiN/TiO_2 composite photoanodes show higher V_{OC} and *FF* but lower J_{SC} values than those of the DSSC with P25 photoanode. The higher V_{OC} is due to the more negative flat band potential provided by the TiN/TiO_2 composite film containing higher TiN content; the higher *FF* is due to higher conductivity of the TiN/TiO_2 composite film containing higher TiN content.

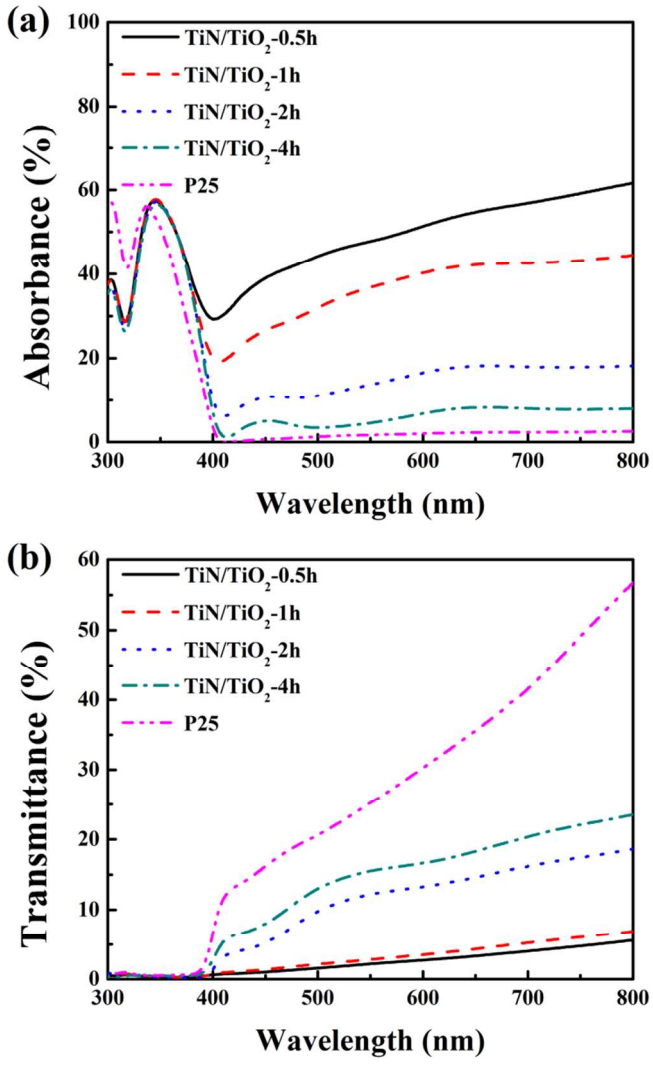

Fig. 3 UV-visible-NIR spectra of the films for (a) absorption and (b) transmittance.

It will be proved in further discussions through Mott–Schottky plots that all TiN/TiO_2 composite films have more negative flat-band potentials than that of P25. However, with increasing annealing period, the increasing TiO_2 content in the photoanodes contributes to the more preferable surface area for the dye adsorption, thus the J_{SC} values of their DSSCs increases. In the schematic summary in **Scheme 1**, there are three key factors affecting the efficiency of a DSSC, including the flat band potential, conductivity, and dye loading amount of the TiN/TiO_2 composite photoanode. Therefore, the best DSSC with the TiN/TiO_2-1h photoanode exhibits a power conversion efficiency (η) of 7.27% with V_{OC} of 784 mV, J_{SC} of 12.68 mA cm^{-2}, and *FF* of 0.70, and it provides higher cell efficiency than that of the standard cell with P25 photoanode.

Under dark condition, the higher onset bias for the dark current of a DSSC implies the better suppression of charge recombination, and thereby the higher V_{OC} for the DSSC. The values of onset bias were obtained from the intersection points of two fitting lines: one is the tangent to the curve starting from the voltage scale; the other is the zero-current line. In **Fig. 4b**, the onset bias values for the dark currents of the DSSCs with TiN/TiO_2-0.5h, TiN/TiO_2-1h, TiN/TiO_2-2h, TiN/TiO_2-4h, and P25 photoanodes can be found at 719, 701, 679, 656, and 656 mV, respectively. With increasing annealing time, the onset bias values decrease, which is in a great consistency with the corresponding decreasing V_{OC} values. Similar results can be clearly seen from the plots of logarithmic dark current density versus applied voltage for the DSSCs with different photoanodes, as shown in **Fig. S6**. Therefore, the introducing of TiN/TiO_2 composite photoanodes is a proper approach for improving the V_{OC} and preventing the electron recombination in a DSSC.

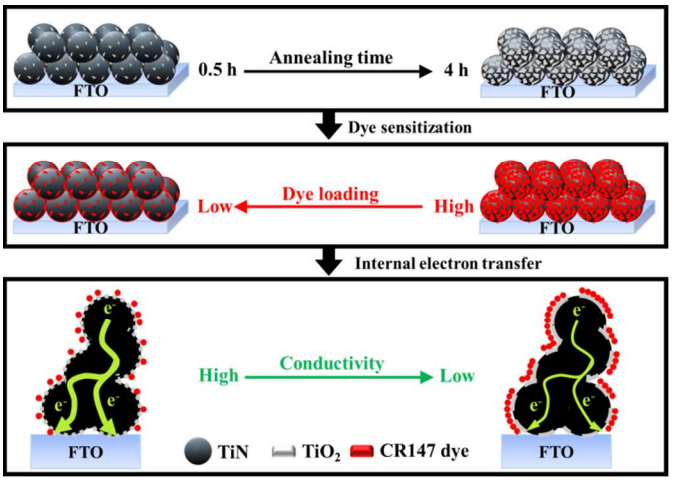

Scheme 1. A schematic summary of the key factors that influence the DSSC performance.

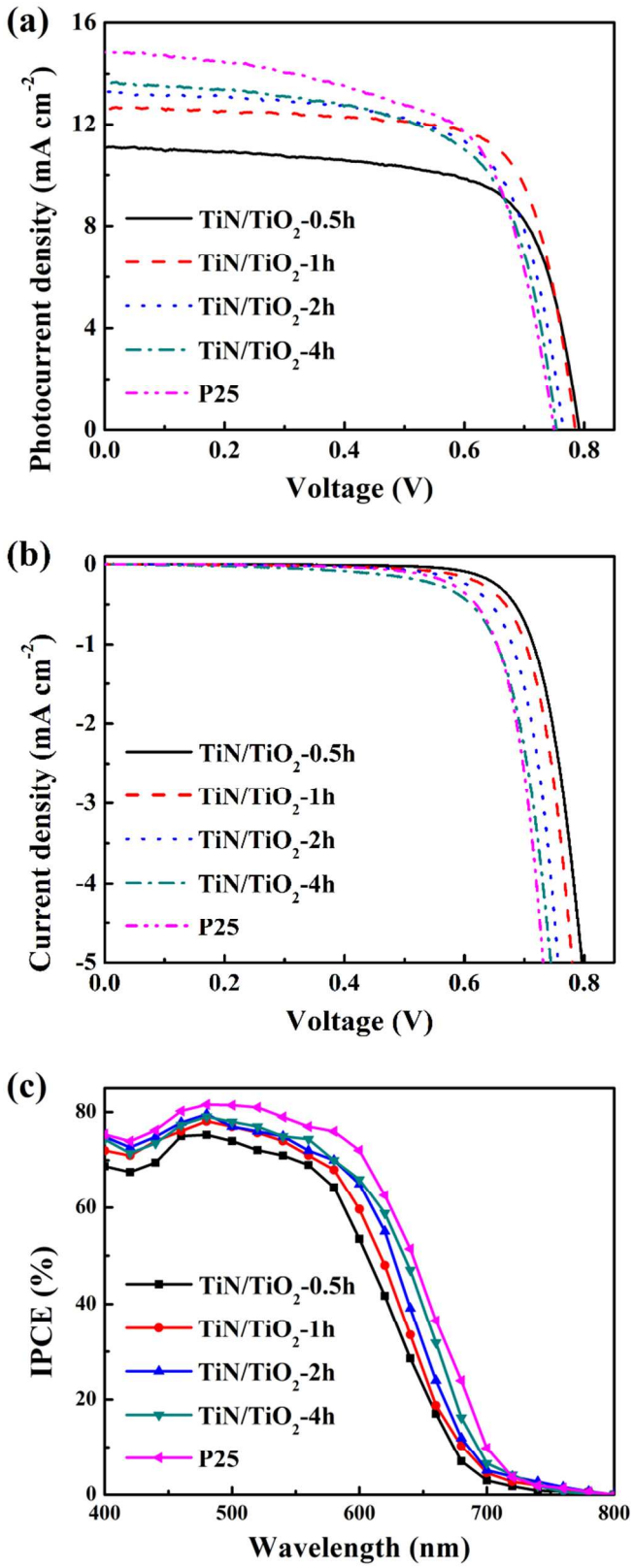

Fig. 4 Current density–voltage curves of the DSSCs with various photoanodes, measured at (a) 100 mW cm^{-2} (AM 1.5G) and (b) dark condition. (c) Incident photon–to–current conversion efficiency curves of the DSSCs with various photoanodes.

Fig. 4c shows incident photon–to–current conversion efficiency (IPCE) curves of the DSSCs with different photoanodes. The maximum IPCE values of the DSSCs with TiN/TiO_2-0.5h, TiN/TiO_2-1h, TiN/TiO_2-2h, TiN/TiO_2-4h, and P25 photoanodes at 480 nm are 75.30%, 78.11%, 79.56%, 79.06%, and 81.60%, respectively. It is well known that the higher the IPCE is, the higher the J_{SC} becomes. The under-lined area of an IPCE curve can be further integrated to calculate the theoretical short–circuit current density, $(J_{SC})_{IPCE}$, of the pertinent DSSC. In **Table 1**, the $(J_{SC})_{IPCE}$ values were summarised and showed a great consistency with the J_{SC} values obtained from the *J-V* curves.

Electrochemical impedance spectra of the DSSCs

Electrochemical impedance spectra of the DSSCs with different photoanodes were used to explain the DSSCs performance mentioned above. Under 100 mW cm^{-2} light illumination, the charge transfer resistance (R_{ct2}) and electron recombination life time (τ_e) can be used to investigate the charge transfer phenomenon at the photoanode/electrolyte interface; those values can be obtained by fitting the impedance data to an equivalent circuit[62], which is presented as the inset of **Fig. 5a**. In **Fig. 5a**, the R_{ct2} value of a DSSC can be obtained from the diameter of the second semicircle in its Nyquist plot, measured at lower frequencies (10–100 Hz range). In **Fig. 5b**, the electron life time (τ_e) of a DSSC can be calculated from its Bode plot by applying the frequency value at the maxima phase (f_{max}) into Eqn. (1)[62].

$$\tau_e = (2\pi f_{max})^{-1} \quad (1)$$

Table 1 gives the values of R_{ct2} and τ_e for different DSSCs with different photoanodes. A larger R_{ct2} value implies the lesser charge passes through the photoanode/electrolyte interface, and thereby a lower current density for the DSSC. **Table 1** shows that the trend of J_{SC} values is consistent with that of R_{ct2} values. A larger τ_e value implies a better retardation for the electron recombination with I^-/I_3^- redox couple, and thereby a higher V_{OC} value for the DSSC. Table 1 also shows the consistent tendency between the V_{OC} values and the τ_e values.

Under dark condition, the charge recombination resistance (R_{rec}) at the photoanode/electrolyte interface can be measured at the applied potential of -0.80 V, which is close to the V_{OC} value obtained in this work. In **Fig. 5c**, the R_{rec} value of a DSSC can be estimated from the diameter of the second semicircle in its Nyquist plot, measured at lower frequencies (10–100 Hz range)[62]. A higher R_{rec} value implies a better suppression for the electron recombination with I^-/I_3^- redox couple, and thereby a higher V_{OC} value for the DSSC. It can be seen in **Table 1** that the V_{OC} values are in consistency with the R_{rec} values.

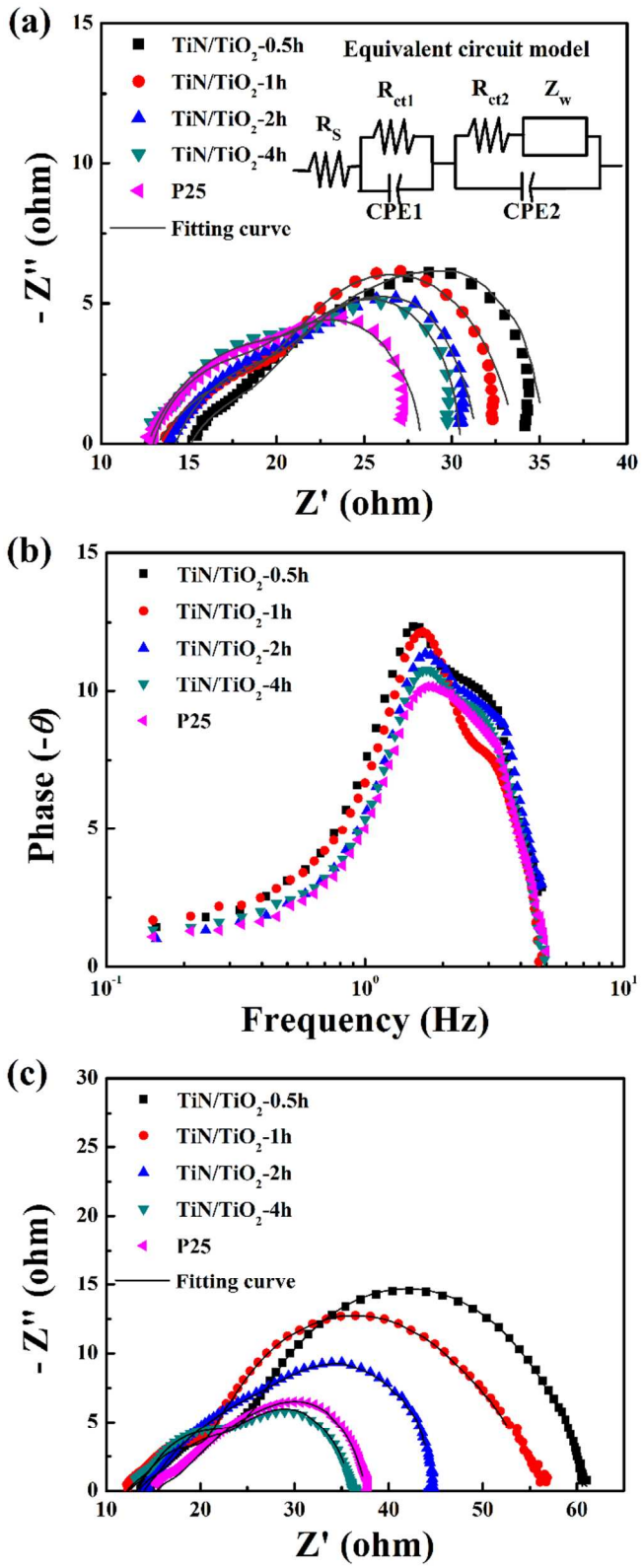

Fig. 5 (a) Nyquist plots and (b) Bode plots of the DSSCs with various photoanodes, measured at 100 mW cm^{-2} (AM 1.5G). (c) Nyquist plots of the DSSCs with various photoanodes, measured under dark condition at an applied potential of -0.80 V.

Water splitting performance

In regard of water splitting reaction under light illumination, when the applied voltage is more positive than the flat-band potential of the photoanode (also as the semiconductors), the photoanode produces both electrons and holes (Eqn. (2)). The holes generated in the valance band (VB) of the photoanode trigger the oxidation of H_2O (Eqn. (3)). At the same time, the electrons produced in the conduction band (CB) of the photoanode trigger the reduction of H_2O, evolving H_2 simultaneously (Eqn. (4))[53]. The standard potentials (E^0) for oxidation of H_2O and reduction of H_2O are at 1.23 V and 0.00 V versus to normal hydrogen electrode, respectively.

$$\text{Photoanode} \xrightarrow{h\nu} e^- (CB) + h^+ (VB) \quad (2)$$

$$2OH^- + 2h^+ \rightarrow \frac{1}{2} O_2 + H_2 \qquad E^0 = 1.23 \text{ V } \textit{vs.} \text{ NHE} \quad (3)$$

$$2H_2O + 2e^- \rightarrow H_2 + 2OH^- \qquad E^0 = 0.00 \text{ V } \textit{vs.} \text{ NHE} \quad (4)$$

The current density–voltage characteristics of the water splitting electrochemical cells coupled with various TiN/TiO_2 composite films as the photoanodes are measured at AM 1.5G (100 mW cm^{-2}) by using a chopping method and shown in **Fig. 6**. Accordingly, the specific photo-induced current density (J_{pho}), which is the difference between the current densities obtained under illumination and dark condition, can be extracted and summarized in **Table 1**. The highest J_{pho} (0.12 mA cm^{-2}) is obtained for the cell with TiN/TiO_2-1h photoanode, which is even higher than that obtained for the device with P25 (0.05 mA cm^{-2}) as shown in **Fig. S7**. For further investigation, we provide the photo-induced current densities of various TiN/TiO_2 composite photoanodes measured under ultraviolet (UV) light illumination, $(J_{pho})_{UV}$, as shown in **Fig. S8**. It is found that the $(J_{pho})_{UV}$ increases steadily (from 0.84 to 3.13 mA cm^{-2}) with increasing the annealing time, due to the increasing TiO_2 proportion in the composite films enhances UV light absorption. Because there is 5% light intensity is contributed by the UV light region in the solar light spectrum at AM1.5G (100 mW cm^{-2}), the higher $(J_{pho})_{UV}$ value of a TiN/TiO_2 composite film may cause the higher J_{pho} value.

On the other hand, the higher TiN proportion in the films brings the more negative flat-band potential for better triggering the H_2O redox. It will be proved in further discussions through the Mott–Schottky plots and corresponding energy diagrams. In summary, there are two key factors affecting the J_{pho} value of the film obtained at AM 1.5G: one is its $(J_{pho})_{UV}$ response, and the other is its flat-band potential. Therefore, the TiN/TiO_2-1h photoanode shows the best water splitting performance with the highest J_{pho} of 0.12 mA cm^{-2}.

Energy band diagram

The energy band diagram of a photoanode can be accomplished by calculating its energy band gap (E_g) via UV-vis-NIR spectrophotometer, followed by measuring its flat-band potential (E_{fb}) via electrochemical impedance spectroscopy. First of all, the energy band gap (E_g) of the photoanode can be obtained by using the its absorption coefficient (α) and the incident photon energy ($h\nu$) in Eqn. (5)[66].

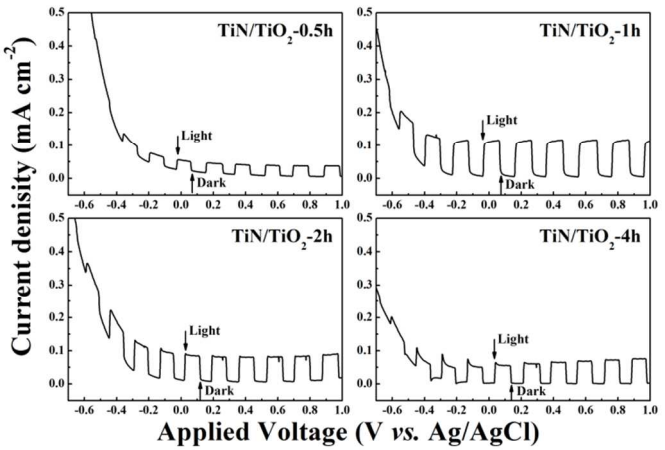

Fig. 6 Photo-induced current density–voltage curves for the electrochemical water splitting cells with various TiN/TiO_2 composite photoanodes, measured at 100 mW cm^{-2} (AM 1.5G).

Table 1. Photovoltaic parameters for the DSSCs and photoelectrochemical parameters for water splitting at various photoanodes

Photoanode	η (%)	V_{OC} (mV)	J_{SC} (mA cm^{-2})	FF	Conductivity (S/cm)	Dye loading (mol cm^{-2})	$(J_{SC})_{IPCE}$ (mA cm^{-2})	R_{ct2} (Ω)	τ_e (ms)	R_{rec} (Ω)	J_{pho} (mA cm^{-2})	$(J_{pho})_{UV}$ (mA cm^{-2})	E_{fb}^{NHE} (V)	E_g (eV)
TiN/TiO_2-0.5h	6.13	792	11.13	0.73	2.29×10^3	1.03×10^{-5}	10.05	11.29	4.63	34.47	0.04	0.84	-0.58	2.88
TiN/TiO_2-1h	7.27	784	12.68	0.70	2.13×10^3	1.37×10^{-5}	11.69	10.66	3.43	29.54	0.12	1.65	-0.34	2.96
TiN/TiO_2-2h	6.83	763	13.35	0.67	1.82×10^3	1.43×10^{-5}	12.29	9.05	3.12	21.97	0.08	2.25	0.14	3.09
TiN/TiO_2-4h	6.62	748	13.67	0.65	1.78×10^3	1.44×10^{-5}	12.68	8.93	2.59	16.41	0.07	3.13	0.24	3.18
P25	7.02	748	14.82	0.63	1.75×10^3	3.17×10^{-5}	13.50	7.87	2.59	16.38	0.05	3.35	0.26	3.20

And the α value of a photoanode can be calculated via its absorption and transmittance spectra (**Fig. 3a** and **3b**), by using the Manifacier model as Eqn. (6)[66, 67].

$$(\alpha h\nu) \propto (h\nu - E_g)^{1/2} \quad (5)$$

$$\alpha = \frac{ln[(A+T)/T]}{film\ thickness} \quad (6)$$

where A is the absorption and T is the transmittance of the film. According to the plot of $(\alpha h\nu)^2$ versus $h\nu$ as shown in **Fig. 7a**, the value of E_g of a photoanode can be determined by extrapolating the tangent line of the plot to $(\alpha h\nu)^2 = 0$. **Table 1** gives that the E_g values of various TiN/TiO_2 composite films range from 2.88 to 3.18 eV for different annealing periods. The E_g values of TiN/TiO_2-4h and P25 are 3.18 and 3.20 eV, respectively, which agree well with the E_g of pure TiO_2[67]. It can be observed that the higher TiN content in the films leads to the lower E_g value, which is attributed to that the higher TiN content provides the more visible light absorption, better conductivity, and more efficient photoelectron–hole separation[20, 21]. For a DSSC, the lower E_g value indicates the better conductivity of the photoanode, and causes the higher *FF* value of the DSSC. As for water splitting, the lower E_g value implies the more efficient photoelectron–hole separation, and gives the higher J_{pho} values of TiN/TiO_2 composite films than that of P25 film.

Secondly, the E_{fb} value of a photoanode can be read from the Mott–Schottky plots of corresponding electrochemical impedance spectra (EIS). The Mott–Schottky plots can be obtained by plotting the reciprocal of the root of the capacitance (C^{-2}) versus the applied voltage (E). At a high frequency of 10 kHz, the equivalent circuit of a semiconductor/electrolyte interface can be simplified to a resistance–capacitance (RC) circuit, and the E_{fb} of a photoanode can be determined from the slope and intercept of the fitting line of its Mott–Schottky plot, by using the Mott–Schottky equation[68] (Eqn. (7)).

$$\frac{1}{C^2} = \left[\frac{2}{q\epsilon\epsilon_0 N_D A^2}\right]\left[E - E_{fb} - \frac{kT}{q}\right] \quad (7)$$

where k is Boltzmann constant, T is the absolute temperature, C is the capacitance of the space-charge of the film, ε is the dielectric constant of the film, ε_0 is the permittivity of the vacuum, A is the surface area of the film (1 cm^2), N_D is the charge density of the film, q is its electric charge, E is the applied voltage to it, and E_{fb} is the flat-band potential of the film.

In **Fig. 7b**, the slopes of Mott–Schottky plots of all photoanodes are positive, which confirms that all photoanodes are n-type semiconductors in this study. As summarized in **Table 1**, the E_{fb} values of the photoanodes are in the range of -0.33 to 0.51 V *vs.* normal hydrogen electrode (NHE). The more the TiN content in a photoanode, the more negative E_{fb} value can be observed. For a DSSC, the more negative E_{fb} value causes larger difference between the Fermi level of the photoanode and the redox potential of I^-/I_3^-, so that the V_{OC} value of the DSSC enlarge. For water splitting, the more negative E_{fb} value provides larger driving force to trigger the H_2O redox. It can be further explained by the energy band diagram (**Fig. 8**) of all photoanodes, which is determined by using the corresponding E_g, E_{fb}, conduction band potential (E_c), and valance band potential (E_v) values of the films. Based on the previous report[69], the E_c value of a photoanode can be calculated from its electron concentration and E_{fb} value, and the E_v value is extracted from the E_c and E_g value accordingly. In **Fig. 8**, the more negative E_{fb} values indicate more negative E_c values of the TiN/TiO_2 composite photoanodes. Considering the E^0 for H_2 production in Eqn. (3), more negative E_c values of the TiN/TiO_2 composite films imply larger driving forces in favor of water splitting, compared to that of P25 film. This explains the higher J_{pho} value in favor of TiN/TiO_2-1h, compared to that of P25, under visible light irradiation.

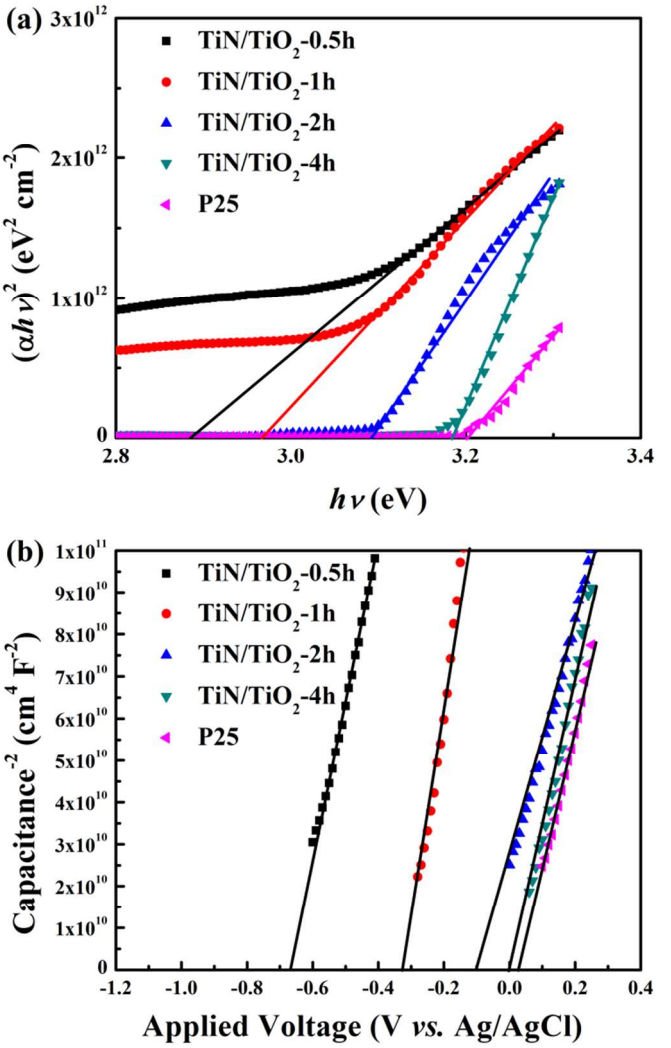

Fig. 7 (a) Plots of $(\alpha h\nu)^2$ *vs.* $h\nu$ for various films; (b) Mott–Schottky plots of various films, obtained by using a neutral 0.5 M K_2SO_4 aqueous electrolyte (pH=7).

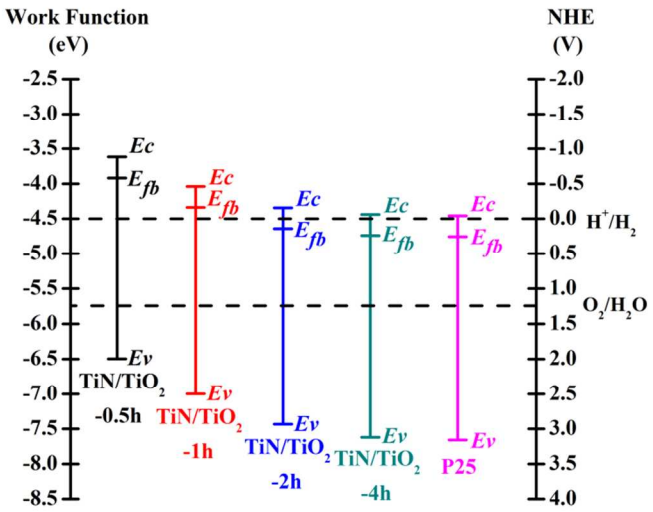

Fig. 8. Energy band diagram of various semiconductor films.

Conclusions

Titanium nitride/titanium oxide (TiN/TiO_2) composite photoanodes were explored for the use in dye-sensitized solar cells (DSSCs) as well as in water splitting. The efficient TiN/TiO_2 composite films possess good uniformity and high porous structure by using a home-made POEM dispersant in a simple doctor blade procedure followed by a post-annealing treatment. By applying thermal treatment at 500 ^{o}C for different periods, TiN cubic crystalline in the TiN precursor films could be partially converted to two tetragonal TiO_2 crystalline, anatase and rutile phases, simultaneously. And the TiN/TiO_2 composite films containing both TiN and TiO_2 crystallines are applied as the photoanodes for the DSSCs or for water splitting separately. Composite films with higher content of TiN show higher absorption of visible light. Moreover, we investigate several key characteristics to determine the performance for both applications, *i.e.*, the conductivity, visible light absorption, energy band gap, or flat-band potential of the films. In the case of DSSCs, an increase in the TiN content in the photoanode leads to increases in the values of V_{OC} and *FF* and a decrease in the value of J_{SC}. The increase in the value of V_{OC} is attributed to a shift in the flat-band potential to a more negative value, the increase in the value of FF is apparently due to the higher conductivity of the film, and the decrease in the J_{SC} value is owing to lesser dye loading caused by lesser content of TiO_2 at a shorter period of annealing. Dark current densities behavior, charge recombination resistance (R_{rec}) values, and electron life time (τ_e) values are used to verify the V_{OC} values. Dye loading data, IPCE, and charge transfer resistance (R_{ct}) values are used to explain the J_{SC} values of the cells. The best DSSC with TiN/TiO_2 composite photoanode annealed for 1 h (TiN/TiO_2-1h) exhibited a power conversion efficiency of 7.27%, while the cell without TiN, *i.e.*, the cell with a P25 photoanode, showed an efficiency of 7.02%. In the case of water splitting, we find that the higher TiN content in a photoanode possesses the more negative flat-band potential for better triggering the H_2O redox, but the less photo-induced current response at UV light illumination. Therefore, considering the water splitting performance measured at AM 1.5G, the TiN/TiO_2-1h composite photoanode shows the best photo-induced current density (J_{pho}) of 0.12 mA cm^{-2}, compared to that of the P25 film. An energy band diagram reveals a higher driving force for water splitting in favor of TiN/TiO_2-1h film, compared to that in favor of P25 film. This explains the higher J_{pho} value in favor of TiN/TiO_2-1h film, compared to that of P25 film, under visible light irradiation. For the best of our knowledge, this is the first report for achieving the highest DSSCs and water splitting performance by applying the highly efficient TiN/TiO_2 composite photoanodes separately. We therefore conclude that both dye-sensitized solar cells and water splitting electrochemical devices would independently achieve their best performance when the TiN/TiO_2 composite photoanode was annealed for 1 h.

Acknowledgements

This work was sponsored by the Ministry of Science and Technology (MOST) of Taiwan. We also would like to acknowledge the financial supports received from the Ministry of Economic Affairs of Taiwan (101-EC-17-A-08-S1-205 and 102-EC-17-A-08-S1-205).

Notes and references

[a] Department of Chemical Engineering, National Taiwan University, No. 1, Sec. 4, Roosevelt Road, Taipei 10617, Taiwan.
[b] Institute of Chemistry, Academia Sinica, No. 128, Sec. 2, Academia Road, Nankang District, Taipei 115, Taiwan.
[c] Institute of Polymer Science and Engineering, National Taiwan University, No. 1, Sec. 4, Roosevelt Road, Taipei 10617, Taiwan.
*Corresponding author: E–mail: kcho@ntu.edu.tw, sssun@chem.sinica.edu.tw, and jianglin@ntu.edu.tw

† Footnotes should appear here. These might include comments relevant to but not central to the matter under discussion, limited experimental and spectral data, and crystallographic data.

Electronic Supplementary Information (ESI) available: [details of any supplementary information available should be included here]. See DOI: 10.1039/b000000x/

1. J. X. Xue, G. J. Zhang, L. P. Guo, H. B. Zhang, X. G. Wang, J. Zou, S. M. Peng and X. G. Long, *J. Eur. Ceram. Soc.*, 2014, **34**, 633.
2. T. Ogi, R. Balgis, K. Okuyama, N. Tajima and H. Setyawan, *Inorg. Mater.*, 2013, **59**, 2753.
3. X. Zhou, F. Peng, H. Wang, H. Yu and J. Yang, *Mater. Res. Bull.*, 2011, **46**, 840.
4. D. Demirskyi, D. Agrawal and A. Ragulya, *J. Alloys Compd.*, 2013, **581**, 498.
5. S. Saadati, A. Salimi, R. Hallaj and A. Rostami, *Sens. Actuators B*, 2014, **191**, 625.
6. M. Sun, P. Song, J. Li and X. Cui, *Mater. Res. Bull.*, 2013, **48**, 4271.

7. Z. Zhang, J. B. M. Goodall, D. J. Morgan, S. Brown, R. J. H. Clark, J. C. Knowles, N. J. Mordan, J. R. G. Evans, A. F. Carley, M. Bowker and J. A. Darr, *J. Eur. Ceram. Soc.*, 2009, **29**, 2343.
8. M. M. Solovan, V. V. Brus, P. D. Maryanchuk, M. I. Ilashchuk, J. Rappich, N. Nickel and S. L. Abashin, *Semicond. Sci. Technol.*, 2014, **29**, 015007.
9. S. Ohya, B. Chiaro, A. Megrant, C. Neill, R. Barends, Y. Chen, J. Kelly, D. Low, J. Mutus, P. J. J. O'Malley, P. Roushan, D. Sank, A. Vainsencher, J. Wenner, T. C. White, Y. Yin, B. D. Schultz, C. J. Palmstrøm, B. A. Mazin, A. N. Cleland and J. M. Martinis, *Supercond. Sci. Technol.*, 2014, **27**, 015009.
10. H. G. Leduc, B. Bumble, P. K. Day, B. H. Eom, J. Gao, S. Golwala, B. A. Mazin, S. McHugh, A. Merrill, D. C. Moore, O. Noroozian, A. D. Turner and J. Zmuidzinas, *Appl. Phys. Lett.*, 2010, **97**, 102509.
11. M. Sandberg, M. R. Vissers, J. S. Kline, M. Weides, J. Gao, D. S. Wisbey and D. P. Pappas, *Appl. Phys. Lett.*, 2012, **100**, 262605.
12. C. J. Yang and F. H. Lu, *Langmuir*, 2013, **29**, 16025.
13. P. Pedrosa, D. Machado, C. Lopes, E. Alves, N. P. Barradas, N. Martin, F. Macedo, C. Fonseca and F. Vaz, *Appl. Surf. Sci.*, 2013, **285**, 40.
14. A. P. Serro, C. Completo, R. Colaço, F. dos Santos, C. L. da Silva, J. M. S. Cabral, H. Araújo, E. Pires and B. Saramago, *Surf. Coat. Tech.*, 2009, **203**, 3701.
15. X. Chen, *Int. J. Quantum Chem.*, 2013, **113**, 2295.
16. K. Feng and Z. Li, *Thin Solid Films*, 2013, **544**, 224.
17. Z. Cui, R. G. Burns and F. J. DiSalvo, *Chem. Mater.*, 2013, **25**, 3782.
18. R. Kumar, S. Pasupathi, B. G. Pollet and K. Scott, *Electrochim. Acta*, 2013, **109**, 365.
19. E. K. Lee, J. K. Kim, T. J. Kim, H. Song, J. H. Kim, S. A. Park, T. G. Jeong, S. W. Yun, J. Lee, J. Goo, J. H. Kim, B. G. Park, H. H. Chun, P. K. Song, C. G. Kang and Y. T. Kim, *Energy Convers.*, 2013, **75**, 727.
20. G. Li, P. Zhang, Z. Bian, J. Zhu, L. Wu and H. Li, *ChemSusChem*, 2013, **6**, 1461.
21. S. Chen, Y. Yang and W. Liu, *J. Hazard. Mater.*, 2011, **186**, 1560.
22. J. M. Lee, S. B. Han, Y. J. Song, J. Y. Kim, B. Roh, I. Hwang, W. Choi and K. W. Park, *Appl. Catal. A*, 2010, **375**, 149.
23. K. Maeda, B. Lee, D. Lu and K. Domen, *Chem. Mater.*, 2009, **21**, 2286.
24. Y. Xie, Y. Wang and H. Du, *Mater. Sci. Eng. B*, 2013, **178**, 1443.
25. C. Xia, Y. Xie, Y. Wang, W. Wang, H. Du and F. Tian, *J. Appl. Electrochem.*, 2013, **43**, 1225.
26. X. Zhou, C. Shang, L. Gu, S. Dong, X. Chen, P. Han, L. Li, J. Yao, Z. Liu, H. Xu, Y. Zhu and G. Cui, *ACS Appl. Mater. Interfaces*, 2011, **3**, 3058.
27. A. Kardakova, M. Finkel, D. Morozov, V. Kovalyuk, P. An, C. Dunscombe, M. Tarkhov, P. Mauskopf, T. M. Klapwijk and G. Goltsman, *Appl. Phys. Lett.*, 2013, **103**, 252602.
28. J. J. Scragg, T. Kubart, J. T. Wätjen, T. Ericson, M. K. Linnarsson and C. Platzer-Björkman, *Chem. Mater.*, 2013, **25**, 3162.
29. P. Chen and W. Y. Wu, *Surf. Coat. Technol.*, 2013, **231**, 140.
30. J. Park, Y. S. Jun, W. r. Lee, J. A. Gerbec, K. A. See and G. D. Stucky, *Chem. Mater.*, 2013, **25**, 3779.
31. C. Liu, J. An, R. Guo, Y. Li and L. Liu, *J. Alloys Compd.*, 2013, **563**, 33.
32. Y. Qiu, K. Yan, S. Yang, L. Jin, H. Deng and W. Li, *ACS Nano*, 2010, **4**, 6515.
33. L. P. B. Lima, J. A. Diniz, C. Radtke, M. V. P. dos Santos, I. Doi and J. Godoy Fo, *J. Vac. Sci. Technol. B*, 2013, **31**, 052202.
34. C. P. Lee, L. Y. Lin, K. W. Tsai, R. Vittal and K. C. Ho, *J. Power Sources*, 2011, **196**, 1632.
35. Q. W. Jiang, G. R. Li and X. P. Gao, *Chem. Commun.*, 2009, 6720.
36. G. R. Li, F. Wang, Q. W. Jiang, X. P. Gao and P. W. Shen, *Angew. Chem. Int. Ed.*, 2010, **49**, 3653.
37. M. H. Yeh, L. Y. Lin, C. P. Lee, H. Y. Wei, C. Y. Chen, C. G. Wu, R. Vittal and K. C. Ho, *J. Mater. Chem.*, 2011, **21**, 19021.
38. E. Ramasamy, C. Jo, A. Anthonysamy, I. Jeong, J. K. Kim and J. Lee, *Chem. Mater.*, 2012, **24**, 1575.
39. X. Zhang, X. Chen, S. Dong, Z. Liu, X. Zhou, J. Yao, S. Pang, H. Xu, Z. Zhang, L. Li and G. Cui, *J. Mater. Chem.*, 2012, **22**, 6067.
40. H. Xu, X. Zhang, C. Zhang, Z. Liu, X. Zhou, S. Pang, X. Chen, S. Dong, Z. Zhang, L. Zhang, P. Han, X. Wang and G. Cui, *ACS Appl. Mater. Interfaces*, 2012, **4**, 1087.
41. M. H. Yeh, L. Y. Lin, C. P. Lee, C. Y. Chou, K. W. Tsai, J. T. s. Lin and K. C. Ho, *J. Power Sources*, 2013, **237**, 141.
42. F. Y. Ouyang and W. L. Tai, *Appl. Surf. Sci.*, 2013, **276**, 563.
43. B. O'Regan and M. Grätzel, *Nature*, 1991, **353**, 737.
44. Y. Li, H. Wang, Q. Feng, G. Zhou and Z. Wang, *Energy Environ. Sci.*, 2013, **6**, 2156.
45. A. Pandikumar and R. Ramaraj, *J. Renew. Sust. Energy*, 2013, **5**, 043101.
46. S. H. Hwang, J. Roh and J. Jang, *Chem. Eur. J.*, 2013, **19**, 13120.
47. K. T. Dembele, G. S. Selopal, C. Soldano, R. Nechache, J. C. Rimada, I. Concina, G. Sberveglieri, F. Rosei and A. Vomiero, *J. Phys. Chem. C*, 2013, **117**, 14510.
48. Y. Q. Zhang, D. K. Ma, Y. G. Zhang, W. Chen and S. M. Huang, *Nano Energy*, 2013, **2**, 545.
49. G. Cheng, M. S. Akhtar, O. B. Yang and F. J. Stadler, *ACS Appl. Mater. Interfaces*, 2013, **5**, 6635.
50. C. P. Lee, P. Y. Chen, R. Vittal and K. C. Ho, *Phys. Chem. Chem. Phys.*, 2010, **12**, 9249.
51. S. Morita, T. C. Wei, M. Ikegami and T. Miyasaka, *J. Power Sources*, 2013, **240**, 753.
52. B. Yoo, K. J. Kim, Y. H. Kim, K. Kim, M. J. Ko, W. M. Kim and N. G. Park, *J. Mater. Chem.*, 2011, **21**, 3077.
53. T. Bak, J. Nowotny, M. Rekas and C. C. Sorrell, *Int. J. Hydrogen Energy*, 2002, **27**, 991.
54. K. W. Cheng and C. H. Yeh, Int. *J. Hydrogen Energy*, 2012, **37**, 13638.
55. X. Tang, Q. Tay, Z. Chen, Y. Chen, G. K. L. Goh and J. Xue, *J. Mater. Chem. A*, 2013, **1**, 6359.
56. X. Li, W. Lu, W. Dong, Q. Chen, D. Wu, W. Zhou and L. Chen, *Nanoscale*, 2013, **5**, 5257.
57. Y. Li, T. Takata, D. Cha, K. Takanabe, T. Minegishi, J. Kubota and K. Domen, *Adv. Mater.*, 2013, **25**, 125.
58. R. X. Dong, S. Y. Shen, H. W. Chen, C. C. Wang, P. T. Shih, C. T. Liu, R. Vittal, J. J. Lin and K. C. Ho, *J. Mater. Chem. A*, 2013, **1**, 8471.

59. L. Y. Chang, C. P. Lee, K. C. Huang, Y. C. Wang, M. H. Yeh, J. J. Lin and K. C. Ho, *J. Mater. Chem.*, 2012, **22**, 3185.
60. S. R. Li, C. P. Lee, H. T. Kuo, K. C. Ho and S. S. Sun, *Chem. Eur. J.*, 2012, **18**, 12085.
61. S. R. Li, C. P. Lee, C. W. Liao, W. L. Su, C. T. Li, K. C. Ho and S. S. Sun, Tetrahedron, 2014, DOI: 10.1016/j.tet.2014.02.087.
62. Q. Wang, J.-E. Moser and M. Grätzel, *J. Phys. Chem. B*, 2005, **109**, 14946.
63. M. B. Cortie, J. Giddings and A. Dowd, *Nanotechnology*, 2010, **21**, 115201.
64. U. Guler, J. C. Ndukaife, G. V. Naik, A. G. Nnanna, A. V. Kildishev, V. M. Shalaev and A. Boltasseva, *Nano Lett.*, 2013, **13**, 6078.
65. G. V. Naik, J. L. Schroeder, X. Ni, A. V. Kildishev, T. D. Sands and A. Boltasseva, *Opt. Mater. Express*, 2012, **2**, 478.
66. J. C. Manifacier, M. D. Murcia and J. P. Fillard, *Thin Solid Films*, 1977, **41**, 127.
67. A. Hagfeldt and M. Grätzel, *Chem. Rev.*, 1995, **95**, 49.
68. A. J. Nozik and R. Memming, *J. Phys. Chem.*, 1996, **100**, 13061.
69. W. J. Chun, A. Ishikawa, H. Fujisawa, T. Takata, J. N. Kondo, M. Hara, M. Kawai, Y. Matsumoto and K. Domen, *J. Phys. Chem. B*, 2003, **107**, 1798.

Graphical Abstract

Efficient Titanium Nitride/Titanium Oxide Composite Photoanodes for Dye-Sensitized Solar Cells and Water Splitting

Chun–Ting Li,[a] Sie–Rong Li,[b] Ling–Yu Chang,[c] Chuan–Pei Lee,[a] Pei–Yu Chen,[a] Shih–Sheng Sun,[b,*] Jiang–Jen Lin,[c,*] R. Vittal,[a] and Kuo–Chuan Ho[a,c,*]

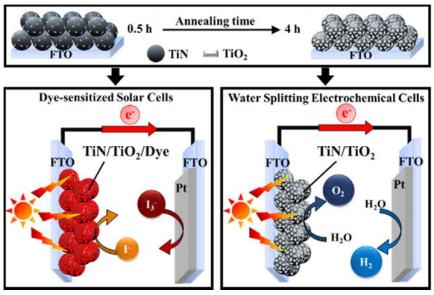

Efficient titanium nitride/titanium oxide composite photoanode separately renders good performance to a dye-sensitized solar cell and a water splitting electrochemical device.